International Journal of Electrical and Electronic Engineering & Telecommunications Vol. 12, No. 1, January 2023

Stability Assessment of a High-Voltage DC Transmission System Using MIMO- and SISO-Based Impedances

Kazuki Ohuchi*, Amirul F. B. Masod, Syunya Kato, and Yuko Hirase
Department of Electrical, Electronic and Communications Engineering, Toyo University, Kawagoe, Japan
Email: {s16C01901164; s16C01900095; hirase028}@toyo.jp

***Abstract*—Grid-connected inverters used in High-Voltage Direct Current (HVDC) transmission systems, which have become increasingly popular worldwide in recent years, employ a variety of control methods for each frequency band, and resonances can occur between multiple control devices within a device or between multiple devices placed in close proximity. Practical impedance-based data-driven methods, rather than linear approximation models, are becoming widely used for these stability analyses. On the other hand, HVDC transmission systems require multiple domain transformations between synchronous and stationary reference frames. Therefore, in this study, both Multiple-Input Multiple-Output (MIMO) analysis using impedances on the direct-quadrature (dq) synchronous frame and Single-Input Single-Output (SISO) analysis using positive and negative sequence impedances on the stationary reference frame were performed. Consequently, the two unstable frequencies identified in the eigenvalue trajectories for the dq impedance were also identified within a single Nyquist plot for the sequence domain impedance, validating both the unstable frequencies observed in the dq domain. These frequencies suggest that weak AC systems on the generation side of the HVDC transmission system may be causing instability in the DC transmission lines and AC systems on the demand side. Additionally, the results of this study also suggest that the introduction of an advanced inverter control method, called the Virtual Synchronous Generator (VSG) control method, in the grid-connected inverter on the receiving side may mitigate the effects of having weak AC systems on the generation side.**

***Index Terms*—High-Voltage Direct Current (HVDC) transmission, modular multilevel converter, marginally stable, virtual synchronous generator**

I. Introduction

Power sources based on Renewable Energy Resources (RESs) have gained widespread popularity in interest of developing a carbon-neutral and decarbonized society. Extensive research has been conducted on the development of wind power generation systems using High-Voltage DC (HVDC) transmission systems owing to their potential economic viability if generated on a large scale.

Modular Multilevel Converters (MMCs) are often employed as converters between the DC transmission line and AC grid. However, various advanced inverter control methods have been proposed in recent years to improve AC system stability. The Virtual Synchronous Generator (VSG) control method is the one that uses storage batteries to equip grid-connected inverters with the characteristics of synchronous generators, and the resultant virtual inertia enhances AC grid stability and promotes the introduction of renewable energy sources. Therefore, there is a great possibility of the VSG control method being adopted in future HVDC systems.

However, unlike the induction generators in wind turbines or the synchronous generators in onshore AC power plants, power electronic devices such as MMCs involve high-speed, complex, and unique controls. Additionally, resonances in a wide frequency range, from several Hz to several tens of kHz, are reported within the equipment or between the equipment and grid. Therefore, there is an urgent need for accurate control and stability analysis of HVDC systems in order to improve their robustness.

The eigenvalue analysis method proposed by Hiti et al. [1] using Fourier series expansion with small-signal models is difficult to apply to modern power systems because it does not assume nonlinear elements in the range of a few Hz to several tens of kHz in power electronics equipment. Moreover, since each of the equipment in an HVDC system is provided by different vendors, inverter control specifications are generally not disclosed. To overcome these drawbacks, data-driven and impedance-based stability analysis methods have been developed recently for accurate analysis of HVDC systems.

Although various studies on impedance-based power system analysis have been conducted globally, most of them have focused primarily on the characteristics of specific equipment, such as grid-connected inverters and loads. For example, Belkhayat [2] incorporated impedance-based stability theory in DC circuits into a three-phase AC circuit in a direct-quadrature (dq) synchronous reference frame and found it to be consistent with the results of mathematical model-based eigenvalue analysis. Next, a sequence impedance-based analysis was proposed to apply the Nyquist criterion-based stability discrimination, even for 2×2 matrices representing three-phase AC impedances [3], [4], and subsequently, Rygg *et*

Manuscript received August 3, 2022; revised September 10, 2022; accepted October 14, 2022.
*Corresponding author: Kazuki Ohuchi (email: s36c02100012@toyo.jp).

al. [5]–[7] proved that dq and sequence impedances are equivalent. In [8], an impedance-based analysis was performed in a microgrid (MG) consisting of inverter power supplies equipped with two different advanced inverter control methods (grid-forming and grid-following inverters). The applications of the impedance method have also been further developed, with methods to reduce the computational burden of numerical analysis [9], [10] and analytical results from demonstration tests [11], [12]. Amin et al. extended an inverter-based MG to an HVDC transmission system and performed the eigenvalue analysis [13]-[15]. In [16], a method was proposed to transform the entire AC system into an equivalent scalar impedance on symmetric coordinates. In [17], an impedance-based analysis of the impact of connecting inverters at different points in the existing system was performed, which can be used as a reference for future power system expansion and planning. The three-port method presented in [18], [19] can also easily represent entire complex systems such as mesh and loop systems by connecting the AC and DC impedances.

The impedance method has already been employed in the stability analysis of an actual HVDC transmission system that is currently in operation. At a wind farm owned by the State Grid Corporation of China, impedance-based analysis of wind turbines from several manufacturers was performed using Hardware-in-the-Loop (CHIL) real-time simulation to identify potential sub-synchronous resonances [20]. TenneT, a German transmission system operator, requires manufacturers of offshore wind turbines to perform impedance-based stability analysis using black box electromagnetic transient (EMT) models provided by HVDC equipment vendors [21].

Against the above background, this study will clarify the impact of a weak generation side AC system on the demand side AC system. Assuming that the demand side AC system is going to be connected by a large number of renewables and become more vulnerable in the future, two types of power control for its MMC were applied: a conventional active and reactive power control and VSG control, which can contribute to stabilizing the AC system. A weak system was simulated by varying the Short Circuit Ratio (SCR) of the generation side AC system to compare conventional power control and VSG control. Additionally, the possibility of improving the stability of the entire HVDC system by the VSG control was examined. The Kawasaki topology [22], which is relatively easy to configure, was used for the VSG control. The currents and voltages in each test case were measured from PSCAD/EMTDC simulations and these impedances were calculated using MATLAB.

Two types of impedances were used in the analysis: dq impedance and sequence impedance. The dq impedance was calculated in the same dq-synchronous reference frame as the generator and inverter control, while the sequence impedance was calculated from the positive and negative sequence of signals in the stationary reference frame. Both impedances were MIMO (2×2) impedances in three-phase AC systems. Although the dq MIMO impedance was easily obtained in the same dq domain as the generator and inverter control system, the analysis was slightly complicated because the unstable frequency was represented by two separate eigenvalue loci. Therefore, once the dq MIMO impedance was converted to MIMO sequence impedance, it was further converted to equivalent SISO impedance using the method adopted in [16]. This makes it possible to confirm the unstable frequency of the entire circuit with fewer calculations.

II. Target System and Controls

A. HVDC Transmission System

Fig. 1 presents the topology of a symmetrical monopolar HVDC system. The monopolar HVDC system was commonly used in the early stages of research and practical applications. Although HVDC transmission systems have both bipolar and monopolar configurations, the differences between these configurations are not discussed in this study.

Terminals 1 (T1) and 2 (T2) represent the generation and demand side terminals, respectively. The electric power flows from T1 to T2, without any power storage devices involved. The generator (e.g. wind turbine) is represented by a voltage source (AC_1) and a source impedance (Z_1) in T1, and the distribution system is represented by a voltage source (AC_2) and a source impedance (Z_2) in T2. The T1 and T2 terminals comprise voltage source converters (VSC) MMC_1 and MMC_2, respectively. This study used the VSC HVDC Model Type-4, as defined in CIGRE B4.57 [23]. In both MMC_1 and MMC_2, the number of submodules was 76, and total cell capacitance, arm reactance, and resistance were, 2800μF, 50mH, and 1Ω, respectively. They were connected to the buses BUS_1 and BUS_2 through transformers Tr_1 and Tr_2, respectively.

The source impedances (z_1 and z_2) were assumed to be of the R-R//L type. The SCR of the AC grid in each terminal was calculated using $\mathrm{SCR} = V_{\mathrm{s\_LL}}^2 / (Z_s P_{\mathrm{dc}})$, where $V_{\mathrm{s\_LL}}$ denotes the line-to-line voltage, P_{dc} denotes the rated power of the VSC, and Z_s represents the magnitude of z_1 or z_2 [24]. The transmission line model provided in PSCAD/EMTDC was applied to each of them.

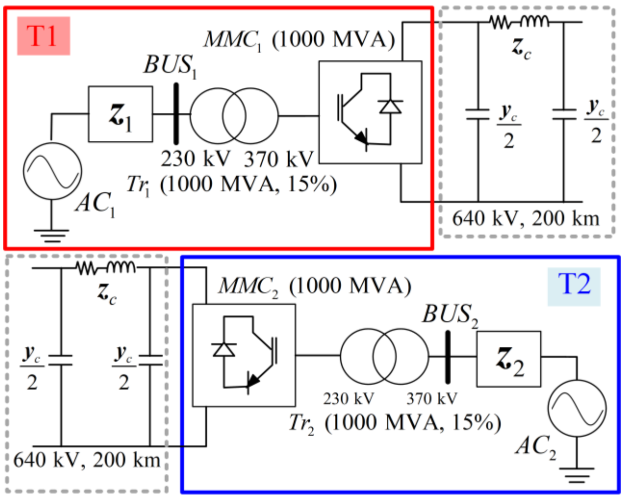

Fig. 1. Topology of a symmetrical monopolar HVDC.

In this study, the overhead line parameters were used for the 400km DC transmission line to simplify the simulation. The 400km DC transmission line was divided into two 200km π type sections, and the series impedance z_c and shunt admittance y_c were set to z_c=(2.122+j0.004) Ω and y_c=–j0.002μΩ, respectively, for every 200km.

B. Voltage and Power Controls

Fig. 2 (a) presents DC voltage control loop in the d-axis and AC voltage control loop in q-axis for MMC$_1$. V_{dc}^* and V_{dc} denote the reference and feedback values of the DC voltage, respectively. Similarly, V_{ac}^* and V_{ac} denote the reference and feedback values of the effective AC voltage (V_{ac}), respectively. Fig. 2 (b) depicts the conventional power control scheme used in MMC$_2$. P and P^* denote the reference and feedback values of the active power, respectively; Q and Q^* denote the reference and feedback values of the reactive power, respectively. The outputs of the voltage and power controllers (i_d^* and i_q^*) were limited to a maximum current reference value of 1.1pu and were fed to the current controller as commands. A non-interference control was used in conjunction with the current control, where ωL=0.2pu. The pulse width modulation (PWM) voltage command vector (V_{abc}^*), obtained from the current controller, was transmitted to the PWM controller. The superscripted "*" values, apart from i_d^* and i_q^*, were assumed to be set in the supervisory control. The transfer functions of V_{dc}, V_{ac}, P, and Q were $H_{Vdc}(s)$=6+(20/s), $H_{Vac}(s)$=0.1+(20/s), $H_P(s)$=0.25+(5/s), and $H_Q(s)$=4+(20/s), respectively. The transfer functions of the current compensators for MMC$_1$ and MMC$_2$ were $H_{cc\_1}(s)$=0.65+(100/s) and $H_{cc\_2}(s)$= 0.6+(10/s), respectively. Here, s denotes the Laplace's differential operator. The value of each parameter was referenced from [25].

Numerical simulations were performed using the PSCAD/EMTDC circuit with the system configuration shown in Fig. 1 and control shown in Fig. 2. An active power load of 750 MW (0.75pu) was connected to BUS$_2$ and the parallel power feeders from both MMCs were tested. MMC$_1$ and MMC$_2$ were deblocked 4s after the simulation was initiated. Both operations were launched

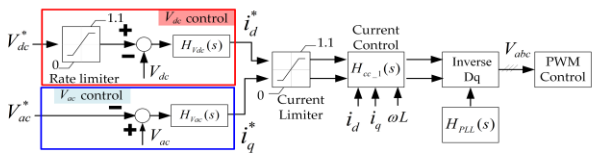

(a)

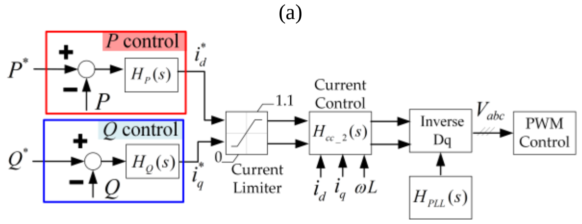

(b)

Fig. 2. Control schemes of MMCs: (a) Voltage control scheme of MMC$_1$ and (b) Power control scheme of MMC$_2$ (Conventional PQ control).

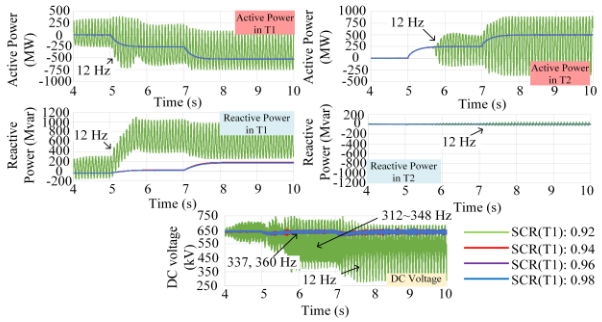

(a)

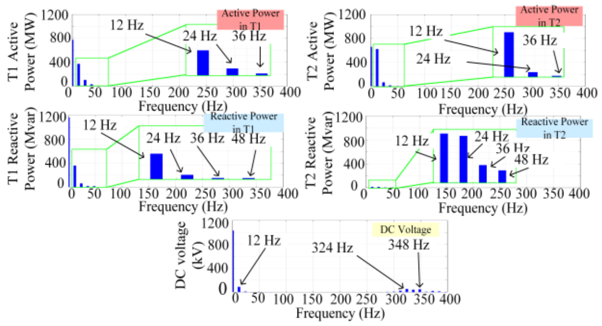

(b)

Fig. 3. Time responses and discrete Fourier transform results with Conventional PQ control: (a) Time response of active/reactive powers and DC voltage and (b) Discrete Fourier transform (DFT) applied to time responses.

with the output power command at P^*=0pu. The output power command was changed to P^*=0.25pu and P^*=0.5pu, respectively, after 5s and 7s into the operation. The impedance Z_1 of AC$_1$ in T1 was varied and its time response was measured. The SCRs of T1 were set to 0.98 (blue), 0.96 (purple), 0.94 (red), and 0.92 (green), while the SCR in T2 was set to 10. Fig. 3 (a) depicts the time responses of active and reactive powers and the time responses of DC voltages. Under the test conditions, when the SCR of T1 dipped below 0.92 (green), the DC voltage control of MMC$_1$ collapsed, affecting the power control of T2. The time response of DC voltage exhibited significant high frequency (324Hz) and low frequency (12Hz) oscillations, while the time response of power showed low frequency (12Hz) oscillations with negligible high frequency (324 Hz) oscillations. Fig. 3 (b) shows the result of applying the discrete Fourier transform (DFT) to the time response of Fig. 3 (a) with an SCR of 0.92 for T1. In all the graphs presented in Fig. 3 (b), in addition to the 12Hz components identified in Fig. 3 (a), 24Hz, 36Hz, and 48 Hz components were also identified. These frequencies represented in the AC powers are values in dq-synchronous reference frame and correspond to 60±12Hz, 60±24Hz, 60±36Hz, and 60±48Hz in stationary reference frames with respect to the fundamental frequency of 60Hz. Similarly, 324Hz in the high-frequency band on the dq-synchronous reference frame indicates (324−60)Hz on the stationary reference frame.

C. VSG Control (Kawasaki Topology)

The power flow control from T1 to T2 in MMC$_2$ assumes that the DC voltage is maintained at a constant value. However, the above tests demonstrate that a weak

AC system in T1 would prevent MMC_1 from maintaining a constant DC voltage and further affect the power control of MMC_2 connected to the strong AC system in T2. Therefore, we employed VSG power control in MMC_2 to observe the variations in the stability of the entire HVDC system and compare them with those of conventional power control methods.

Fig. 4 illustrates the Kawasaki topology of VSG control [22]. ω_c^* and ω_c denote the reference and feedback values of the angular velocity of the AC voltage. ω_c^* was referenced from the supervisory control, whereas ω_c was calculated using the phase-locked loop in the controller. The transfer function of the phase-locked loop (PLL) was $H_{\mathrm{PLL\_vsg}}(s)$=[1/(1+0.016s)]·[20+(125/s)]. The P-F controller (red-framed portion) implemented the virtual swing equation and droop characteristic of ω_c corresponding to P; its transfer function was denoted as $H_{\mathrm{PF}}(s)$. The output of the P-F controller is the phase angle (δ). The Q-V controller (blue-framed portion) implements the droop characteristic of V_{ac} corresponding to Q and acts as the automatic voltage regulator (AVR). The transfer function of the droop characteristic considering the measurement delay was denoted as $H_{\mathrm{QV}}(s)$, and the transfer function of the AVR was denoted as $H_{\mathrm{AVR}}(s)$. The output of the Q-V controller is the electromotive force (E_f). The impedance model (green-framed portion) outputs the current command values (i_d^* and i_q^*). The P-F controller, the Q-V controller, and the impedance model are represented by

$$\delta = \omega_c^* \frac{(P^* - P)H_{\mathrm{PF}}(s)}{s} + \frac{\omega_c^* - \omega_c}{s}, \tag{1}$$

$$|\mathbf{E}_f| = H_{\mathrm{AVR}}(s)((Q^* - Q)H_{\mathrm{QV}}(s) - V_{ac}), \tag{2}$$

$$\mathbf{I}^* = \begin{bmatrix} i_d^* \\ i_q^* \end{bmatrix} = \frac{1}{r^2 + x^2} \begin{bmatrix} r & x \\ -x & r \end{bmatrix} \left(\begin{bmatrix} e_d \\ e_q \end{bmatrix} - \begin{bmatrix} v_d \\ v_q \end{bmatrix} \right). \tag{3}$$

The terms r and x denote the virtual resistance and reactance set in the software, respectively. The AC voltage and electromotive force vectors in the stationary reference (system) frame ($\mathbf{V}_{\mathrm{ac}}$ and $\mathbf{E}_f$) were transformed into the dq-synchronous reference (converter) frame as $\mathbf{V}_{\mathrm{ac}} = [v_d, v_q]^T$ and $\mathbf{E}_f = [e_d, e_q]^T$, respectively. In the VSG control, a non-interference control was not included. In this study, $\omega_c^* = 2\pi 60$ rad/s. The transfer functions of $H_{\mathrm{PF}}(s)$, $H_{\mathrm{QV}}(s)$, and $H_{\mathrm{AVR}}(s)$ were $H_{\mathrm{PF}}(s)$=0.05/(1+0.12s), $H_{\mathrm{QV}}(s)$= 0.05/(1+0.015s), and $H_{\mathrm{AVR}}(s)$=10+80/s, respectively. The transfer function of the current compensator was $H_{\mathrm{cc}}(s)$=0.1+0.2/s in the VSG controller. The virtual impedances were set as r=0.2pu and x=0.4pu, respectively.

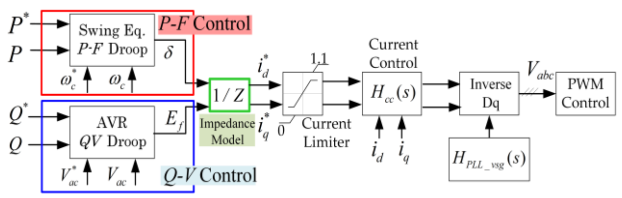

Fig. 4. Control schemes of the VSG control.

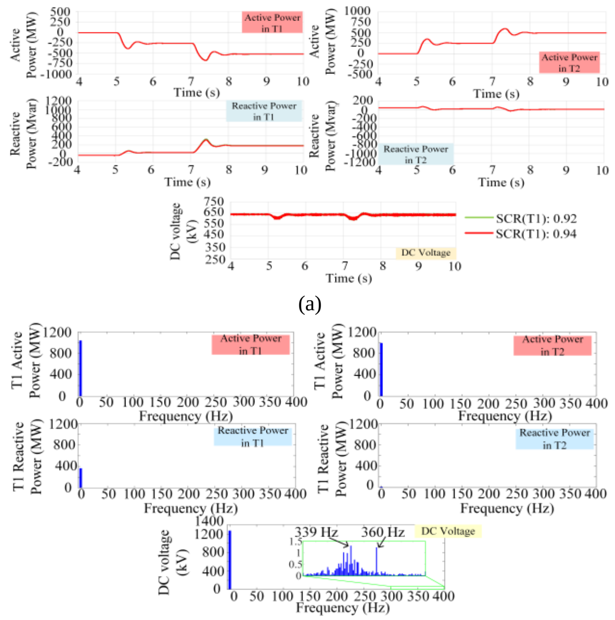

(a)

(b)

Fig. 5. Time responses and discrete Fourier transform results with VSG power control: (a) Time responses with VSG power control and (b) DFT applied to time responses.

Fig. 5 (a) represents the time responses of active and reactive powers and the DC voltage in HVDC systems when VSG power control method was used for MMC_2. Fig. 5 (b) is the result of applying DFT to the time response of Fig. 5(a). The 12 Hz oscillation when using the conventional P-Q control, which was confirmed in Fig. 3, was no longer confirmed in Fig. 5 when VSG control was applied. The high-frequency oscillation of 324 Hz can be seen in the DC voltage in Fig. 5 (a) as well as in Fig. 3 (a). Even though the value of SCR for T1 is the same at 0.92, the 324 Hz oscillation is significantly suppressed in Fig. 5 wherein the VSG control was used for MMC_2. These high-frequency oscillations, which were confirmed in the time responses of the DC voltage, were not confirmed in the AC systems of both terminals in the impedance analysis of this study. Therefore, it was assumed that this oscillation is the inherent frequency of the DC transmission line.

III. Algorithm of System Impedance

A. Analysis on the Dq Synchronous Reference Frame

The detailed derivation of the algorithm used in this study is provided in [7]. In the impedance analysis, the general power system was split between the source and load subsystems. Fig. 6 illustrates Thévenin and Norton equivalents and their block diagrams, respectively. The impedances of the source and load subsystems are $\mathbf{Z}_S(s)$ and $\mathbf{Y}_L(s) = \mathbf{Z}_L^{-1}(s)$. If the system is a DC power system, it can be analyzed using the Nyquist criterion in the minor-loop gain, which is defined as $\mathbf{L}(s)$=$\mathbf{Z}_S(s)\mathbf{Y}_L(s)$. While in the three-phase AC system, the impedance is generally converted from the stationary reference frame to the dq-synchronous reference frame, neglecting the zero-sequence component. Then, the minor-loop gain, given by $\mathbf{L}(s)$=$\mathbf{Z}_S(s)\mathbf{Y}_L(s)$, is a 2×2 matrix in the dq-synchronous reference frame, and subsequently, the generalized Nyquist criterion (GNC) can be applied to **L**(s), similar to the DC system. This indicates that the system stability can be assessed by the condition that the loci of all eigenvalues of the minor-loop gain **L**(s) ($\lambda_1(s)$ and $\lambda_2(s)$), which satisfy (4), do not encircle the point $(-1, j0)$.

$$\det\left(\mathbf{I}+\mathbf{L}(s)\right)=\prod_i\left(1+\lambda_i(s)\right) \tag{4}$$

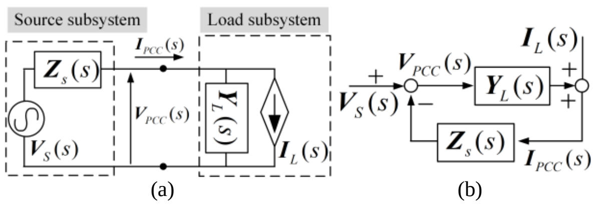

Fig. 6. Splitting of the general power system into source and load subsystems represented by Thévenin and Norton equivalents: (a) Thevenin and Norton equivalents and (b) Block diagram of the equivalent circuit.

B. Analysis on the Sequence Domain

Equation (1) was established in the dq-synchronous reference frame by transforming the three-phase AC system with the Clark-Park transformation and neglecting the zero sequence. When symmetric coordinate transformation was applied to the original three-phase AC system, it was possible to decompose each phase signal into positive, negative, and zero sequences. Similarly, in impedance, the two-phase signal, converted from the three-phase signal, could be decomposed into that sequence domain. In this case, the stability equivalence of the loop gains calculated in the dq-synchronous reference frame and the sequence domain was proved [6], [7].

Let $\mathbf{Z}^{\mathrm{dq}}(s)$ and $\mathbf{Z}^{\mathrm{pn}}(s)$ be the impedances on the dq-synchronous reference frame and the sequence domain, respectively, and $\mathbf{Z}^{\mathrm{dq}}(s)$ and $\mathbf{Z}^{\mathrm{pn}}(s)$ be the minor-loop gains calculated by them, respectively. The relationship between $\mathbf{Z}^{\mathrm{dq}}(s)$ and $\mathbf{Z}^{\mathrm{pn}}(s)$ in the Laplace domain was expressed by (5):

$$\boldsymbol{Z}^{\mathrm{pn}}(s)=\left(\frac{1}{2}\begin{bmatrix}1 & j\\ 1 & -j\end{bmatrix}\right)\boldsymbol{Z}^{\mathrm{dq}}(s)\left(\frac{1}{2}\begin{bmatrix}1 & j\\ 1 & -j\end{bmatrix}\right)^{-1}. \tag{5}$$

Similar to $\mathbf{Z}^{\mathrm{dq}}(s)$, $\mathbf{Z}^{\mathrm{pn}}(s)$ is a 2×2 matrix with the first and second rows representing the phasors of the positive and negative sequences of the d-axis, respectively. As the positive and negative sequences of the q-axis have the same gain and a phase difference of exactly $\pm\pi/2$ rad from those of the d-axis, owing to the nature of symmetric coordinates, it is sufficient to evaluate only (5), which represents the d-axis. Furthermore, the fact that the phasors of the positive and negative sequences are conjugate also simplifies the computation.

Note that the off-diagonal components in $\mathbf{Z}^{\mathrm{pn}}(s)$ still represent that the negative/positive sequence voltages determine the positive/negative sequence currents. That is, even if the sequence impedance is used to represent the source/load impedance, the eigenvalue of the minor loop gain still includes the effect of interference between positive and negative sequences.

Hence, it is possible to convert the impedance of a 2×2 matrix to an equivalent scalar impedance [16]. Here, the MIMO dq impedance was converted to MIMO sequence impedance using equation (2), which was then converted to the equivalent SISO sequence impedance. The subscripts of the matrix represent the source/load subsystem as before, and the superscripts “pp”, “pn”, “np”, and “nn” represent the (1,1), (1,2), (2,1), and (2,2) components of a matrix, respectively. Equations (6) and (7) represent the positive and negative sequence impedances of the entire circuit, and a notable advantage of the method is that these values are scalars.

$$Z^p(s)=Z_S^{\mathrm{pp}}+Z_L^{\mathrm{pp}}-\frac{\left(Z_S^{\mathrm{pn}}+Z_L^{\mathrm{pn}}\right)\left(Z_S^{\mathrm{np}}+Z_L^{\mathrm{np}}\right)}{Z_S^{\mathrm{nn}}+Z_L^{\mathrm{nn}}} \tag{6}$$

$$Z^n(s)=Z_S^{\mathrm{nn}}+Z_L^{\mathrm{nn}}-\frac{\left(Z_S^{\mathrm{pn}}+Z_L^{\mathrm{pn}}\right)\left(Z_S^{\mathrm{np}}+Z_L^{\mathrm{np}}\right)}{Z_S^{\mathrm{pp}}+Z_L^{\mathrm{pp}}} \tag{7}$$

Splitting $Z^P(s)$ between source and load impedances ($Z^P(s)=Z_S^p(s)+Z_L^p(s)$) as expressed in (8) and (9), $Z^n(s)=Z_S^n(s)+Z_L^n(s)$ is easily obtained due to the conjugate relationship ($Z_S^n(s)=\bar{Z}_S^p(s)$, $Z_L^n(s)=\bar{Z}_L^p(s)$).

$$Z_S^p(s)=Z_S^{\mathrm{pp}}-\frac{\left(Z_S^{\mathrm{pn}}\right)\left(Z_S^{\mathrm{np}}+Z_L^{\mathrm{np}}\right)}{Z_S^{\mathrm{nn}}+Z_L^{\mathrm{nn}}} \tag{8}$$

$$Z_L^p(s)=Z_L^{\mathrm{pp}}-\frac{\left(Z_L^{\mathrm{pn}}\right)\left(Z_S^{\mathrm{np}}+Z_L^{\mathrm{np}}\right)}{Z_S^{\mathrm{nn}}+Z_L^{\mathrm{nn}}} \tag{9}$$

In each of (6)–(9), the interference terms were aggregated in the numerator of the fraction in the final term. The loop gains of positive and negative sequences ($\lambda^p(s)$, $\lambda^n(s)$), which were also scalars, were calculated using (10) and (11).

$$\lambda^p(s)=Z_S^p(s)/Z_L^p(s) \tag{10}$$

$$\lambda^n(s)=Z_S^n(s)/Z_L^n(s) \tag{11}$$

It is much easier to analyze the system by using these scalar eigenvalues than to analyze it using the two eigenvalues, including the interphase interference expressed in (4).

IV. Impedance-Based Stability Analysis

In this study, a series voltage perturbation was used in the simulation, and the impedance was calculated from the measured voltage and current. Table I lists the testcases (#1–2) used to measure these values.

TABLE I: THE LIST OF TESTCASES

Case	Perturbation Point	SCR of T1
#1	BUS_1	0.92
#2	BUS_1	0.94

A. HVDC Transmission System with PQ Control for MMC_2

Fig. 7 to Fig. 12 show the results of the impedance-based analyses for the system using the PQ control for MMC_2 in T2.

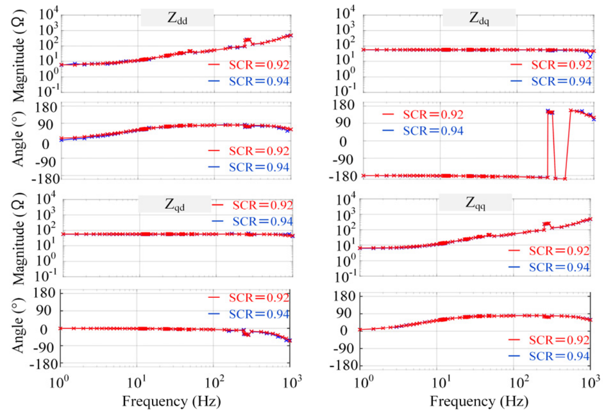

(a)

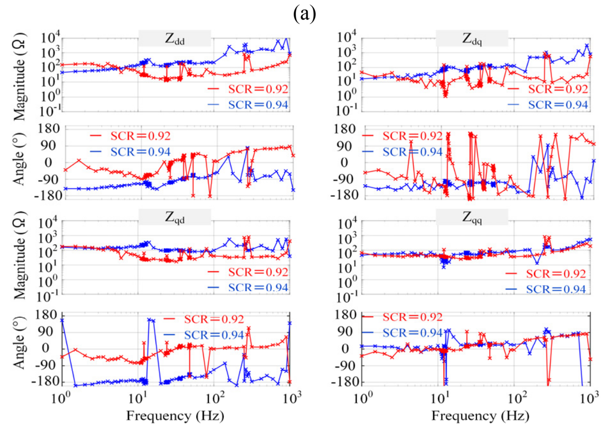

(b)

Fig. 7. dq MIMO impedances of sub-circuits: (a) Output impedance of source-side ($\boldsymbol{Z}_S^{dq}(s)$) and (b) Output impedance of load-side ($\boldsymbol{Z}_L^{dq}(s)$).

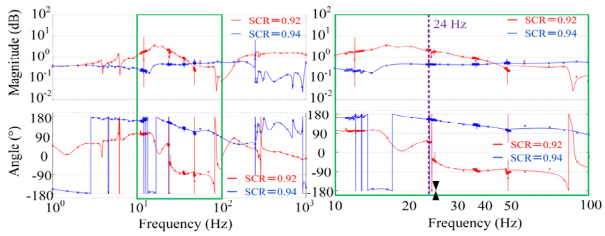

(a)

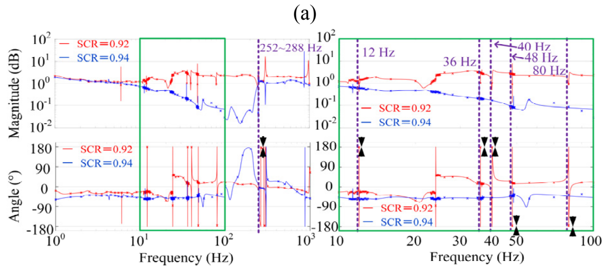

(b)

Fig. 8. Bode plots of the eigenvalues of the MIMO minor-loop gain: (a) Bode plots of λ_1 (the right is an enlargement of the left) and (b) Bode plots of λ_2 (the right is an enlargement of the left).

Fig. 7 represents the dq-impedances of the source and load sub-systems $(\boldsymbol{Z}_S^{\text{dq}}(s), \boldsymbol{Z}_L^{\text{dq}}(s))$, where $\boldsymbol{Z}_S^{\text{dq}}(s)$ and $\boldsymbol{Z}_L^{\text{dq}}(s)$ represent the impedances of T1 and HVDC system side (MMC$_1$, DC line, MMC$_2$, and T2), respectively. The results of #1–2 are represented in red and blue colors, respectively. Fig. 8 and Fig. 9 show the Bode and Nyquist plots of the two eigenvalues ($\lambda_1(s)$ and $\lambda_2(s)$) of the minor-loop gain matrix ($L(s)=Z_S(s)Y_L(s)$), respectively. Fig. 8 (a) and Fig. 9 (a) show the results with regard to λ_1, and Fig. 8 (b) and Fig. 9 (b) depict the results with regard to λ_2.

In each of Fig. 8 (a) and Fig. 8 (b), the right figure is an enlargement of the 10Hz to 100Hz range of the left figure. In Fig. 8 and Fig. 9, the cross markers show the values calculated from the measured data, and solid lines show the estimated transfer functions obtained using MATLAB.

Fig. 10 shows the equivalent SISO impedances calculated using (8) and (9), and the results for #1 and #2 are color-coded similar to the MIMO impedance results. Fig. 10 (a) and Fig. 10 (b) show the output impedances of the source and load sub-systems ($\boldsymbol{Z}_S^{\text{pn}}(s)$, $\boldsymbol{Z}_L^{\text{pn}}(s)$), and the left and right graphs of both figures represent the impedances in the positive and negative sequences, respectively. The positive and negative sequence impedances are conjugate complex relationships and only one of them can be used to determine its properties.

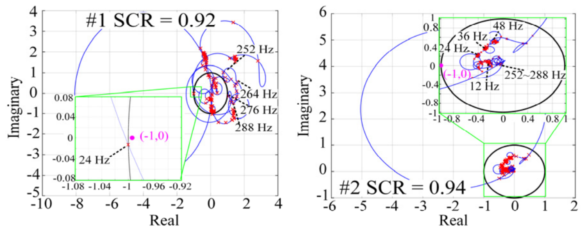

(a)

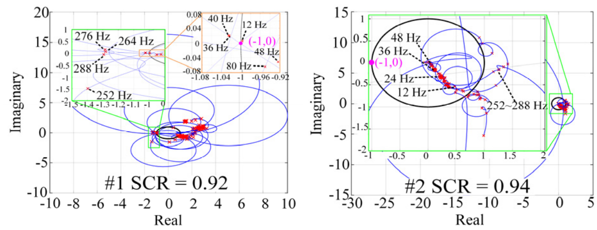

(b)

Fig. 9. Nyquist plots of the eigenvalues of the MIMO minor-loop gain: (a) Eigenvalue loci of λ_1 and (b) Eigenvalue loci of λ_2.

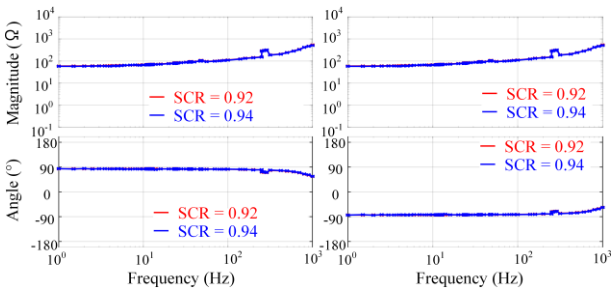

(a)

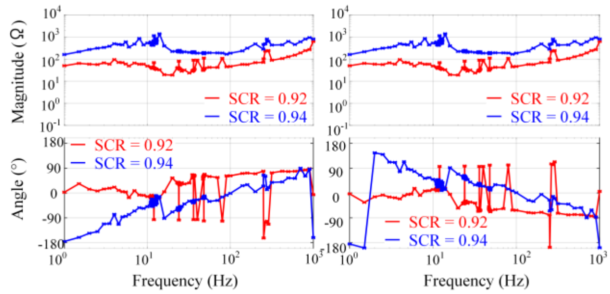

(b)

Fig. 10. Equivalent SISO impedance of sub-circuits: (a) Source-side impedance ($\boldsymbol{Z}_S^{pn}$) and (b) Load-side impedance ($\boldsymbol{Z}_L^{pn}$).

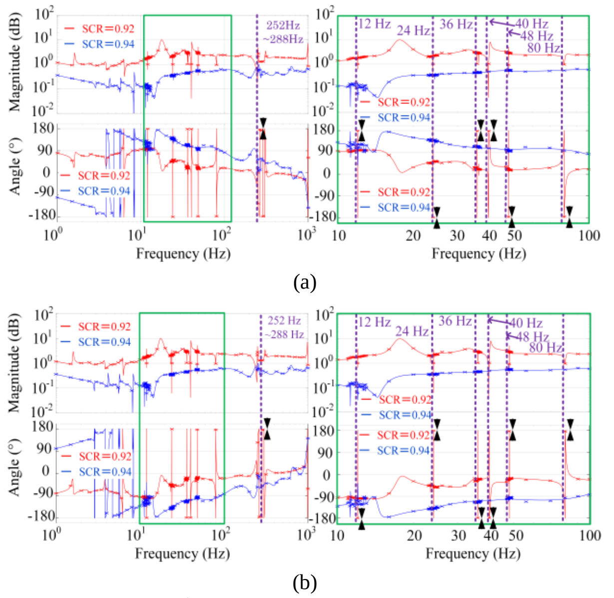

Fig. 11. Bode plots of the eigenvalues SISO minor-loop gain: (a) Bode plots of λ_p (The right is an enlargement of the left) and (b) Bode plots of λ_n (The right is an enlargement of the left).

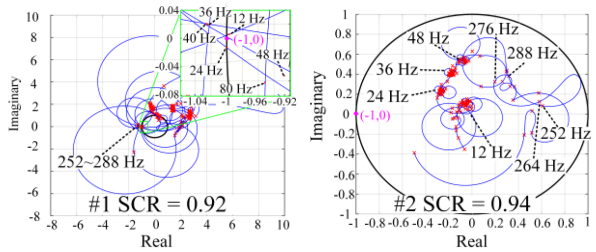

Fig. 12. Eigenvalue loci of the SISO minor-loop gain.

Fig. 11 and Fig. 12 show the Bode and Nyquist plots of the loop gains of positive and negative sequences ($\lambda^p(s)$ and $\lambda^n(s)$) calculated using (10) and (11), respectively. In each of Fig. 11 (a) and Fig. 11 (b), the right figure is an enlargement of the 10Hz to 100Hz range of the left figure. $\lambda^p(s)$ and $\lambda^n(s)$ are conjugate values, only the eigenvalue locus of $\lambda^p(s)$ is shown in Fig. 12.

The minor loop gain calculated from the impedances of the two sub-circuits (Fig. 7) is represented by a MIMO (2×2) matrix in the dq reference frame, and its two eigenvalues should be used to determine the stability (Fig. 8 and Fig. 9). In contrast, the equivalent SISO impedances (Fig. 10) are scalar values, and the minor loop gain of their ratio can be used to intuitively understand the stability (Fig. 11 and Fig. 12). Comparing Fig. 7 with Fig. 10 or Fig. 8 and Fig. 9 with Fig. 11 and Fig. 12, the positive (or negative) sequence impedance in Fig. 10 and the positive (or negative) sequence eigenvalues in Fig. 11 and Fig. 12 consolidate the information of the four different impedances in Fig. 7 and the two eigenvalues of the loop gains in Fig. 8 and Fig. 9, respectively.

In Fig. 7 (a) and Fig. 10 (a), there is no difference between #1 and #2. On the contrary, in Fig. 7 (b) and Fig. 10 (b), although the characteristic gain peaks of 12Hz, 24Hz, 36Hz, and 48Hz are seen in #1, these gain peaks disappear in #2. This indicates that the PQ control of MMC_2 became unstable due to the unstable DC voltage caused by the weak AC_1. Fig. 8, Fig. 9, Fig. 11, and Fig. 12 also show that the unstable low frequencies of 12Hz, 24Hz, 36Hz, and 48Hz are exhibited only in #1. These results clearly agree with those shown in Fig. 3. In Fig. 8 (a) and Fig. 9 (a) (results of $\lambda_1(s)$), the locus of 24Hz shows the possibility of instability, and in Fig. 8 (b) and Fig. 9 (b) (results of $\lambda_2(s)$), 12Hz, 36Hz, and 48 Hz can be seen as unstable frequencies. By contrast, both Fig. 11 and Fig. 12 (results of $\lambda^p(s)$ or $\lambda^n(s)$) show that these four frequencies can be represented at once in a single Bode or Nyquist diagram. In addition to the four frequencies listed above, 40Hz and 80Hz are also identified in Fig. 8, Fig. 9, Fig. 11, and Fig. 12 and are considered candidates for unstable frequencies. However, these frequencies were not identified in Fig. 3. Additional investigation is needed to determine if these frequencies are actually potential unstable frequencies.

The high-frequency oscillation frequencies of the DC voltages of 312Hz, 324Hz, 336Hz, and 348Hz when the SCR of T1 is 0.92 in Fig. 3 correspond to 252Hz, 264Hz, 276Hz, and 288Hz in the synchronous reference frame, and they can be seen around the point (-1, $j0$) in the eigenvalue loci of Fig. 9 and Fig. 12. These frequencies are located farther from the abovementioned point than the low-frequency oscillation frequencies (12Hz, 24Hz, 36Hz, and 48Hz) seen in the AC powers in Fig. 3; this implies that the possibility of these unstable frequencies are also indicated by the AC impedance. However, as described in a previous work [14], in an AC system at BUS_1, which was used as the split point, the unstable frequencies on the DC transmission line may have been canceled out and obscured in the loop gain. Therefore, detailed analysis should be performed using the DC perturbation. Moreover, these frequencies are also error factors in the estimated transfer function of MATLAB, and the accuracy of the estimation should be improved.

B. HVDC Transmission System with VSG Control for MMC_2

Similar to Fig. 7 to Fig. 12, Fig. 13 to Fig. 18 illustrate the results for the impedance-based analyses of the system when the VSG control was implemented in MMC_2. Fig. 13 represents the dq (MIMO) impedances of the source and load sub-systems ($\boldsymbol{Z}_S^{dq}(s)$, $\boldsymbol{Z}_L^{dq}(s)$), and Fig. 14 and Fig. 15 represent the Bode and Nyquist plots of the two eigenvalues ($\lambda_1(s)$ and $\lambda_2(s)$) of the minor-loop gain matrix ($\boldsymbol{L}(s) = \boldsymbol{Z}_S(s)\boldsymbol{Y}_L(s)$), respectively.

Fig. 16 represents the equivalent SISO impedances ($\boldsymbol{Z}_S^{pn}(s)$, $\boldsymbol{Z}_L^{pn}(s)$), and Fig. 17 and Fig. 18 represent the Bode and Nyquist plots of eigenvalues ($\lambda^p(s)$ and $\lambda^n(s)$), respectively. Both the low-frequency unstable frequencies (12Hz, 24Hz, 36Hz, 40Hz, 48Hz, and 80Hz) and high-frequency unstable frequencies (252Hz, 264Hz, 276Hz, and 288Hz), which were seen when PQ control was used for MMC_2 with an SCR of 0.92 for T1, were not identified as unstable frequencies in the impedances, Bode plots, and Nyquist plots (MIMO, SISO) when VSG control was used for MMC_2.

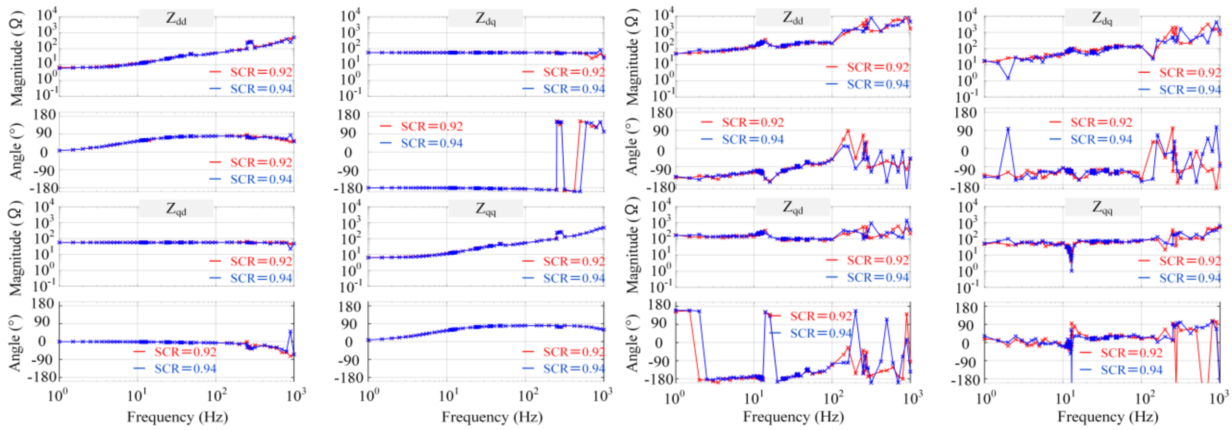

(a) (b)

Fig. 13. dq MIMO impedances of the sub-circuits, using the VSG control for MMC$_2$ in T2: (a) Output impedance of source-side ($\boldsymbol{Z}_S^{dq}(s)$) and Output impedance of load-side ($\boldsymbol{Z}_L^{dq}(s)$).

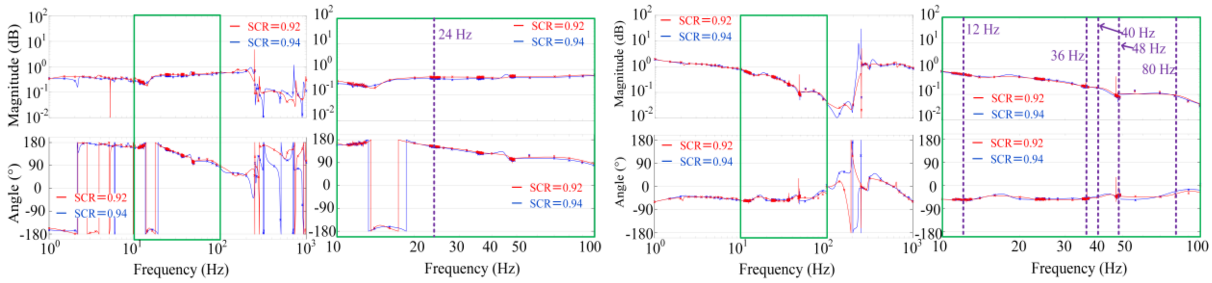

(a) (b)

Fig. 14. Bode plots of the eigenvalues of the dq MIMO minor-loop gain, using the VSG control for MMC$_2$ in T2: (a) Bode plots of λ_1 (The right is an enlargement of the left) and (b) Bode plots of λ_2 (The right is an enlargement of the left).

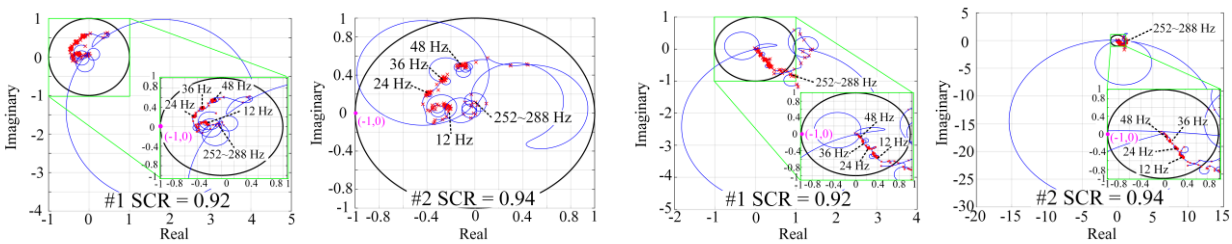

(a) (b)

Fig. 15. Nyquist plots of the eigenvalues of the dq MIMO miner loop gain, using the VSG control for MMC$_2$ in T2: (a) Eigenvalue loci of λ_1 and (b) Eigenvalue loci of λ_2.

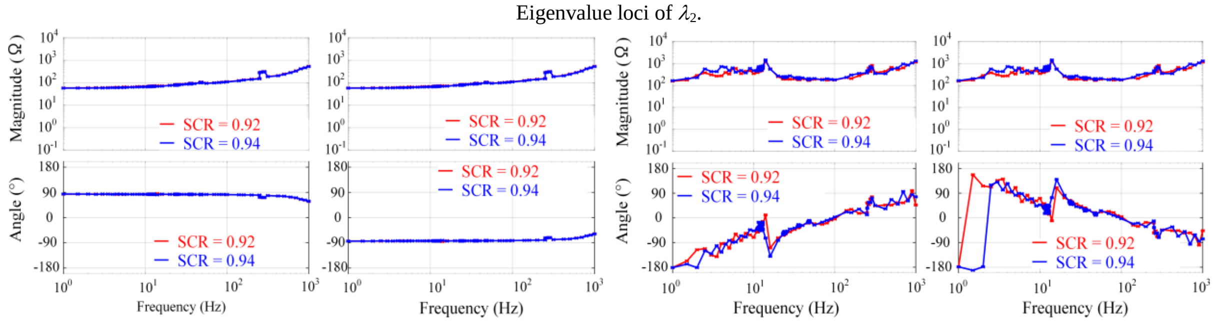

(a) (b)

Fig. 16. Equivalent SISO impedance of sub-circuits, using the VSG control for MMC_2 in T2: (a) Source-side impedance ($\boldsymbol{Z}_S^{pn}$) and (b) Load-side impedance ($\boldsymbol{Z}_L^{pn}$).

Conventional PQ and VSG controls are power controls placed in the upper layer of the same minor current loop control, and their frequency bands are typically 0.1 to several Hz. The unstable frequencies of 12Hz, 24Hz, 36Hz, and 48Hz on the synchronous reference frame (48Hz, 36Hz, 24Hz, and 12Hz on the stationary reference frame) identified in the above test results were located in a slightly higher frequency band than that of the power control frequency band. Therefore, the differences of the results may originate from the fact that the VSG control applied in this study intentionally sets the PLL and current controller gains as low to enable uninterruptible transition between stand-alone and grid-connected operation.

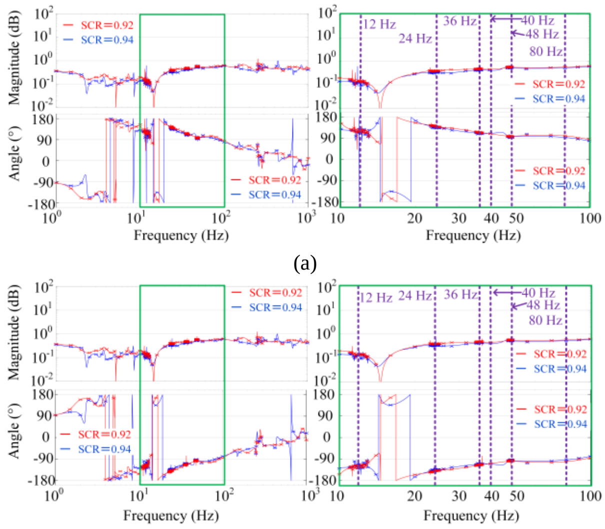

(a)

(b)

Fig. 17. Bode plots of the eigenvalues SISO minor-loop gain, using the VSG control for MMC_2 in T2: (a) Bode plots of λ_p (the right is an enlargement of the left) and (b) Bode plots of λ_n (the right is an enlargement of the left).

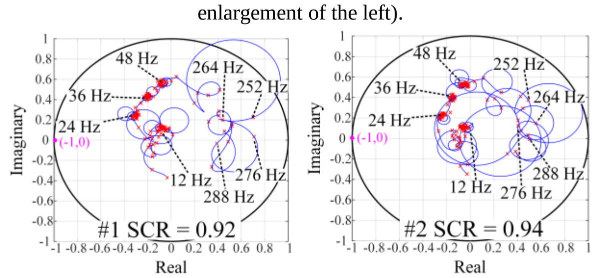

Fig. 18. Eigenvalue loci from the minor-loop gain derived from the SIO impedance, using the VSG control for MMC_2 in T2.

V. Conclusion

In this study, impedance-based stability analysis was applied to an entire HVDC transmission system to evaluate the impedance and stability of different control methods. It was found that when the SCR of the generation-side AC system was smaller than a threshold value, the use of conventional power control on the demand-side AC system caused unstable oscillations in the DC voltage, which further affected the demand-side AC system. In contrast, it was confirmed that the application of VSG control, which has a grid stabilizing effect, to the demand-side AC system significantly suppressed oscillations in DC voltage and stabilized the demand-side AC system. However, this study only analyzed the AC system on the generation side, so further research is needed to investigate the DC section.

Moreover, the equivalent SISO impedance of the entire circuit was calculated, and the stability was verified using the system that was connected to the demand-side AC system via a VSG-controlled inverter. Equivalent scalar impedance allowed for a more intuitive interpretation of physical phenomena in the positive and negative sequences. Seeking clarification on ways to improve the scalar impedance characteristics expressed in positive and negative sequences by adjusting the VSG parameters on the dq coordinate is our future venture.

The VSG control employed in this study implemented the GFM-type Kawasaki topology, which is characterized by simulated synchronous generator characteristics that can be reproduced relatively easily and a virtual impedance mechanism. Such VSG control is expected to avoid unstable frequencies identified in the impedance-based stability analysis quite easily by employing software-configured virtual impedance. However, sensitivity analysis, by changing the control parameters, to improve the stability margin of the output impedance and mathematical analysis, such as a linear model of VSG control for consistency verification, are not included in this research phase and require continued research in the future. As the current control and PLL in its lower layers affect the response of the power control, it is necessary to carefully diagnose and verify which control variable is responsible for the difference in stabilities of the two power controls (PQ control and VSG control) used in MMC_2.

Conflict of Interest

The authors declare no conflict of interest.

Author Contributions

Y. Hirase conducted the research; A. F. B. Masod, S. Kato, and K. Ohuchi performed the simulations; A. F. B. Masod, S. Kato, and K. Ohuchi conducted the data curation; all authors analyzed the data; all authors wrote the paper; all authors had approved the final version.

Acknowledgment

This work was supported by a grant from JSPS KAKENHI (Grant Number 22K14246) and the INOUE ENRYO Memorial Grant, 2022, TOYO University.

References

[1] S. Hiti, D. Boroyevich, and C. Cuadros, “Small-signal modeling and control of three-phase PWM converters,” in *Proc. 1994 IEEE Industry Applications Society Annual Meeting*, Denver, 1994, pp. 1143-1150.

[2] M. Belkhayat, “Stability criteria for AC power systems with regulated loads,” Ph.D. dissertation, Dept. Elect. Eng., Purdue Univ., West Lafayette, IN, US, 1997.

[3] J. Sun, “AC power electronic systems: stability and power quality,” in *Proc. 2008 11th Workshop on Control and Modeling for Power Electronics*, Zurich, 2008, pp. 1-10.

[4] J. Sun, “Small-signal methods for AC distributed power systems–A review,” *IEEE Trans. on Power Electronics*, vol, 24, no. 11, pp. 2545-2554, Nov. 2009.

[5] A. Rygg, M. Molinas, E. Unamuno, C. Zhang, and X. Cai, “A simple method for shifting local dq impedance models to a global reference frame for stability analysis,” *arXiv*:1706.08313v1, 2017

[6] A. Rygg, M. Molinas, C. Zhang, and X. Cai, “On the equivalence and impact on stability of impedance modeling of power electronic converters in different domains,” *IEEE Journal of Emerging and Selected Topics in Power Electronics*, vol., 5, no. 4, pp. 1444-1454, Dec. 2017.

[7] A. Rygg, “Impedance-based methods for small-signal analysis of systems dominated by power electronics,” Ph.D. dissertation, Dept. Engineering Cybernetics, Norwegian University of Science and Technology, Trondheim, Norway, 2018.

[8] E. Unamuno, A. Rygg, M. Amin, M. Molinas, and J. A. Barrena, “Impedance-based stability evaluation of virtual synchronous

machine implementations in converter controllers," in *Proc. 2018 Int. Power Electronics Conf.*, Niigata, 2018, pp. 759-766.
[9] H. Mao, D. Boroyevich, and F. C. Lee, "Novel reduced-order small-signal model of a three-phase PWM rectifier and its application in control design and system analysis," *IEEE Trans. on Power Electronics*, vol. 13, no. 3, pp. 511-521, May 1998.
[10] L. Harnefors, M. Bongiorno, and S. Lundberg, "Input-admittance calculation and shaping for controlled voltage-source converters," *IEEE Trans. on Industrial Electronics*, vol. 54, no. 6, pp. 3323-3334, Dec. 2007.
[11] G. Francis, R. Burgos, D. Boroyevich, F. Wang, and K. Karimi, "An algorithm and implementation system for measuring impedance in the DQ domain," in *Proc. 2011 IEEE Energy Conversion Congress and Exposition*, Phoenix, 2011, pp. 3221-3228.
[12] J. Sun, "Impedance-based stability criterion for grid-connected inverters," *IEEE Trans. on Power Electronics*, vol. 26, no. 11, pp. 3075-3078, Nov. 2011.
[13] M. Amin and M. Molinas, "Self-Synchronisation of wind farm in MMC-based HVDC system," in *Proc. 2016 IEEE Electrical Power and Energy Conf.*, Ottawa, 2016, pp. 1-6.
[14] M. Amin and M. Molinas, "Small-signal stability assessment of power electronics-based power systems: A discussion of impedance-and eigenvalue-based methods," *IEEE Trans. on Industry Applications*, vol. 53, no. 5, pp. 5014-5030, Sept.-Oct. 2017.
[15] M. Amin and M. Molinas, "A gray-box method for stability and controller parameter estimation in HVDC-connected wind farms based on nonparametric impedance," *IEEE Trans. on Industrial Electronics*, vol. 66, no. 3, pp. 1872-1882, March 2019.
[16] C. Zhang, X. Cai, A. Rygg, and M. Molinas, "Sequence domain SISO equivalent models of a grid-tied voltage source converter system for small-signal stability analysis," *IEEE Trans. on Energy Conversion*, vol. 33, no. 2, pp. 741-749, June 2018.
[17] A. Firdaus and M. Molinas. (2020). Design and expansion planning of parallel inverter based AC microgrids - An approach for improved stability margins. [Online]. Available: https://doi.org/10.36227/techrxiv.12894926.v1
[18] H. Zong, C. Zhang, X. Cai and M. Molinas, "Three-port impedance model and validation of VSCs for stability analysis," in *Proc. 2021 Annual Meeting of CSEE Study Committee of HVDC and Power Electronics*, Hybrid (China), 2021, pp. 293-298.
[19] H. Zong, C. Zhang, X. Cai, and M. Molinas, "Analysis of power electronics-dominated hybrid AC/DC grid for data-driven oscillation diagnosis," in *Proc. 2022 Int. Power Electronics Conf.*, Himeji, 2022, pp. 2328-2333.
[20] B. Liu, Z. Li, X. Zhang, X. Dong, and X. Liu, "Impedance-based analysis of control interactions in weak-grid-tied PMSG wind turbines," *IEEE Journal on Emerging and Selected Topics in Circuits and Systems*, vol. 11, no. 1, pp. 90-98, March 2021.
[21] Offshore-Netzanschlussregeln O-NAR, TenneT TSO GmbH, Arnhem. The Netherlands. (Aug. 2019). [Online]. Available: https://www.tennet.eu/fileadmin/user_upload/The_Electricity_Market/German_Market/Grid_customers/NAR_Offshore_2019.pdf
[22] Y. Hirase, K. Abe, K. Sugimoto, K. Sakimoto, H. Bevrani, and T. Ise, "A novel control approach for virtual synchronous generators to suppress frequency and voltage fluctuations in microgrids," *Applied Energy*, vol. 210, pp. 699-710, Jan. 2018.
[23] R. Wachal, A. Jindal, S. Dennetiere, H. Saad, O. Rui, S. Cole, *et al*., "Guide for the development of models for HVDC converters in a HVDC grid," Cigré WG B4, pp. 27-32, 2014.
[24] D. Jovcic, *High Voltage Direct Current Transmission: Converters, Systems and DC grids*, 2nd ed, Wiley, 2019, ch. 9, pp. 95-98.
[25] HVDC VSC transmission interconnecting two AC systems. [Online]. Available: pscad.com/knowledge-base/article/222.

Copyright © 2023 by the authors. This is an open access article distributed under the Creative Commons Attribution License (CC BY-NC-ND 4.0), which permits use, distribution and reproduction in any medium, provided that the article is properly cited, the use is non-commercial and no modifications or adaptations are made.

Kazuki Ohuchi received his B.Eng. degree in electrical, electronic, and communications engineering from Toyo University, Kawagoe, Saitama, Japan, in 2021. He is currently studying power electronics, distributed power systems, and energy storages in his master's course.

Amirul F. B. Masod received his diploma in electrical and electronic engineering from University Kuala Lumpur Malaysia Italy Design Institute, Kuala Lumpur, in 2021. Since 2021, he has been enrolled in the Department of Electrical, Electronic and Communication Engineering, Toyo University, Kawagoe, Saitama, Japan. He is studying power electronics and impedance-based system analysis.

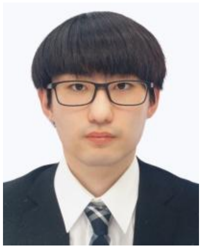

Shunya Kato is enrolled in electrical, electronic, and communications engineering at Toyo University, Kawagoe, Saitama, Japan, since 2019. He is currently studying power electronics and impedance-based system analysis.

Yuko Hirase received her M.Eng. degree in mathematical engineering from Osaka Prefecture University, Sakai, Osaka, Japan, in 1996 and her Ph.D. degree in electrical engineering from Osaka University, Suita, Osaka, Japan, in 2016. From 2006 to 2019, she worked for Kawasaki Technology Co., Ltd. She is working as an associate professor at Toyo University, Kawagoe, Saitama, Japan, since 2019. Since 2022, she is also a technical committee member of Electricity and Gas Market Surveillance under the Ministry of Economy, Trade, and Industry. Her research interests include microgrids, distributed generation, synchronous generators, and power conversion systems. Additionally, she is also involved in the design and development of power inverters for renewable energies and system stabilizers. She is a senior member of IEEE, and a member of CIGRE, IEEJ, and JIPE.